A Global Classification Dataset of Daytime and Nighttime Marine Low-cloud Mesoscale Morphology Based on Deep Learning Methods

Yuanyuan Wu[1], Jihu Liu[2,3], Yannian Zhu[1,2,3,*], Yu Zhang[2], Yang Cao[2,3], Kang-En Huang[2], Boyang Zheng[2], Yichuan Wang[2], Yanyun Li[2], Quan Wang[2], Chen Zhou[2], Yuan Liang[4], Jianning Sun[2], Minghuai Wang[2,3], Daniel Rosenfeld[2,5]

[1]Nanjing-Helsinki Institute in Atmospheric and Earth System Sciences, Nanjing University, Nanjing, 210023, China
[2]School of Atmospheric Sciences, Nanjing University, Nanjing, 210023, China
[3]Joint International Research Laboratory of Atmospheric and Earth System Sciences & Institute for Climate and Global Change Research, Nanjing, 210023, China
[4]TianJi Weather Science and Technology Company, Beijing, 100000, China
[5]Institute of Earth Sciences, The Hebrew University of Jerusalem, Jerusalem 91904, Israel
Correspondence to: Yannian Zhu (yannian.zhu@nju.edu.cn)

Abstract. Marine low clouds tend to organize into larger mesoscale patterns with distinct morphological appearances over the ocean, referred to as mesoscale morphology. While prior studies have mainly examined the fundamental characteristics and shortwave radiative effects of these mesoscale morphologies, their behaviour in the nighttime marine boundary layer (MBL) remains underexplored due to limited observations. To address this, we established a global classification dataset of daytime and nighttime marine low-cloud morphology using a deep residual network model and infrared radiance data of 1°×1° resolution from the Moderate Resolution Imaging Spectroradiometer (MODIS), with machine-learning-retrieved all-day cloud optical thickness aiding in model training. We analysed day-night contrasts in climatology, seasonal cycles, and cloud properties of different cloud morphology types in this study. Results show that relative frequency of occurrence of closed mesoscale cellular convection (MCC) significantly increase at night, while that of suppressed cumulus (Cu) shows a remarkable decrease. Disorganized MCC and clustered Cu display a slight frequency increase during night. In addition, solid stratus and three MCC types exhibit distinct seasonal variations, whereas two cumuliform types show no clear seasonal cycle. Our dataset extends the study of mesoscale cloud morphologies from daytime to nighttime and $1^{o} \times 1^{o}$ resolution makes it better match with other climate datasets. It will provide an important foundation for further research on the interactions between cloud morphology and climate processes. The final cloud classification dataset ~~Our dataset~~ as well as the model development datasets ~~is~~ are open-access and available at https://doi.org/10.5281/zenodo.13801408 (Wu et al., 2024).

1 Introduction

Marine low clouds cover the vast area of oceans and have a pronounced impact on the Earth's radiation budget. They exert a strong radiative cooling on the planet as the residual of a larger cooling effect and a positive warming effect (Klein and Hartmann, 1993; Eytan et al., 2020). These radiative effects are known to be sensitive to cloud types due to their different cloud properties, such as cloud fraction and albedo. Traditional ground-based observations have classified individual marine low clouds using the cloud types defined by the World Meteorological Organization (WMO), such as cumulus (Cu), stratocumulus (Sc) and stratus (St) (Zhang et al., 2018; Li et al., 2022; Guzel et al., 2024). However, satellite imagery shows that these individual clouds tend to organize into larger mesoscale patterns with distinct morphological features that are not easily discernible from the limited perspective of ground observation instruments. These mesoscale cloud patterns, referred to as cloud mesoscale morphologies, have been shown to exert different radiative effects on climate (McCoy et al., 2017; McCoy et al., 2023; Mohrmann et al., 2021), and also reflect the intricate physical processes of the underlying marine boundary layer (MBL) (Wood, 2012; Bony et al., 2020; Eastman et al., 2022; Liu et al., 2024; Mohrmann et al., 2021).

Previous studies have identified several critical environmental factors that influence the evolution of marine low-cloud morphologies. Open and closed mesoscale cellular convection (MCC) clouds are both affected by cloud-top longwave radiation cooling (Wood, 2012), but the surface fluxes dominate the open MCC when there is a strong cold advection such as polar outbreak. As a result, the passage of mid-latitude cold air outbreaks serve as key triggers for the transition from closed to open MCC (McCoy et al., 2017; Tornow et al., 2021). In the subtropics, precipitation promotes the organization and sustainment of open cell structure and dominates the transformation of closed to open MCC clouds (Savic-Jovcic and Stevens, 2008; Feingold et al., 2010; Yamaguchi and Feingold, 2015; Eastman et al., 2022). In contrast, closed MCC tend to evolve into more disorganized cumulus under conditions of warmer sea surface temperature and increased entrainment of dry air at the cloud top (Eastman et al., 2022; McCoy et al., 2023). Apart from meteorological influences, aerosols are another key cloud-controlling factor (Cao et al., 2024) and can initiate these transitions by modulating precipitation. High aerosol concentration suppresses the precipitation and favors the maintenance of closed MCCs, while the scarcity of aerosols promotes the generation of widespread precipitation, leading to the conversion toward open MCCs (Stevens et al., 2005; Rosenfeld et al., 2006; Petters et al., 2006; Xue et al., 2008; Goren et al., 2019). With global warming and emission reductions, there is a high likelihood that meteorological factors and aerosols will change accordingly. This raises several important questions regarding low-cloud feedback, such as whether the mesoscale morphology of low clouds will change as the climate warms and how these changes will affect radiation.

An objective classification of mesoscale morphology from satellite observations is essential for facilitating a more systematic investigation of these questions. In recent years, deep learning methods, especially those based on convolutional neural networks (CNNs), have proven particularly effective in the objective classification of mesoscale cloud morphology in satellite images. By using a three-layer neural network, Wood and Hartmann (2006) classified daytime cloud morphology at a resolution of 256 × 256 pixels into four categories: no MCC, closed MCC, open MCC, and cellular but disorganized MCC. Their work was pioneering and has since been extended to more than a decade of MODIS observations by McCoy et al. (2023). Yuan et al. (2020) then subdivided the cellular but disorganized category into disorganized MCC, clustered Cu and suppressed Cu for 128 × 128 scenes, and developed a global dataset of these six cloud types using a fine-tuned Visual Geometry Group 16-layer (VGG-16) network. Subsequently, Watson-Parris et al. (2021) employed a pre-trained CNN model to detect pockets of open cells (POCs) (224 × 224 pixel) in three main marine stratocumulus regions during daytime. Moreover, Schulz et al. (2021) developed an object detection model to classify four larger scale (10º×10º) cloud morphologies in trade wind regions of North Atlantic. These morphologies were vividly named as "sugar," "gravel," "flowers," and "fish" mainly based on their visual appearances.

The datasets mentioned above have been utilized for various downstream tasks, such as quantifying shortwave cloud radiative effects and identifying key controlling factors of different cloud morphologies (Bony et al., 2020; Mohrmann et al., 2021; Watson-Parris et al., 2021), quantifying shortwave cloud feedbacks resulting from changes in morphology (McCoy et al., 2023), and investigating aerosol-cloud interactions across different morphologies (Liu et al., 2024). However, most current studies focus on the role of morphology in daytime shortwave radiation, with a notable lack of understanding regarding longwave radiation, particularly nighttime longwave radiation, primarily due to the scarcity of nighttime observations of cloud morphologies. Although a few geostationary satellite-based studies give a nighttime morphological classification, they are also limited to regional scales and lack a global-scale classification dataset (Lang et al., 2022; Segal Rozenhaimer et al., 2023).

The studies on nighttime cloud morphology are limited but essential for investigating cloud-climate feedback. Closed MCC clouds have been shown to peak at night (Lang et al., 2022) and the subsequently increased cloud cover could lead to a rise in surface temperature by enhancing downward longwave radiation (Dai et al., 1999), which would further reduce the diurnal temperature range and affect sea breeze-like circulations (Vose et al., 2005; Davy et al., 2017; Cox et al., 2020). Climate models suggest that, compared to daytime, the slower decline in the long-term trend of nighttime cloud cover could raise the global temperature and amplify climate warming (Luo et al., 2024). However, how these cloud morphology types behave under the influence of the nighttime MBL regime and how nighttime cloud cover varies under different cloud morphology types remain unclear. In addition, marine precipitation is more frequent at night (Dai, 2001; Dai et al., 2007), with its intensity strongly dependent on cloud morphology types (Muhlbauer et al., 2014). Therefore, comparing the differences in cloud morphology between daytime and nighttime may help explain the uneven distribution of precipitation, as well as improve our understanding and prediction of global precipitation changes against the backdrop of climate warming.

Motivated by the aforementioned issues, a new 1° × 1° classification dataset of daytime and nighttime marine low-cloud mesoscale morphology was generated in this study using a residual network model. In contrast to previous cloud classification datasets, our dataset provides global coverage with a temporal resolution of 5 minutes and a spatial resolution of 1º from 2018 to 2022, which makes it better integrate with other standard-grid datasets to deliver more precise information about the meteorological conditions and aerosols. The manuscript is organized as follows. Section 2 introduces the datasets and methods. Section 3 presents the training results and the contents of our dataset. The advantages and limitations of this dataset are discussed in Section 4. Section 5 states the data availability and Section 6 concludes.

2 Data and methods

2.1 Cloud type classifications

We adopted the classification scheme in Yuan et al. (2020) for mesoscale morphological classification of marine low clouds. The examples of each morphology classification are shown in Fig. 1. Solid stratus clouds are driven by cloud-top radiative cooling method and have a flat and uniform surface. Closed MCC clouds are stratocumulus driven by longwave radiative cooling and surface fluxes and display distinctive honeycomb-like structures with clear and descending edges. Open MCCs have a clear descending region in the center, which is surrounded by several active shallow convective clouds. They appear in more unstable environment and typically generate heavier drizzle, lower shortwave reflectance, and greater transmissivity than closed MCC (Wang and Feingold, 2009; Muhlbauer et al., 2014). Disorganized MCC are a mix of convective elements and extensive stratiform clouds, marked by smaller droplets and lower optical thickness (Yuan et al., 2020; Liu et al., 2024). They tend to occur in a drier troposphere and over warmer oceans (Wyant et al., 1997; Bretherton et al., 2019). Clustered Cu refers to the aggregation of shallow, vigorous convective elements, while suppressed Cu consists of individual, scattered cumulus clouds that occasionally form linear or branched patterns. Both of them are frequently observed over warm tropical oceans (Yuan et al., 2020; Mohrmann et al., 2021).

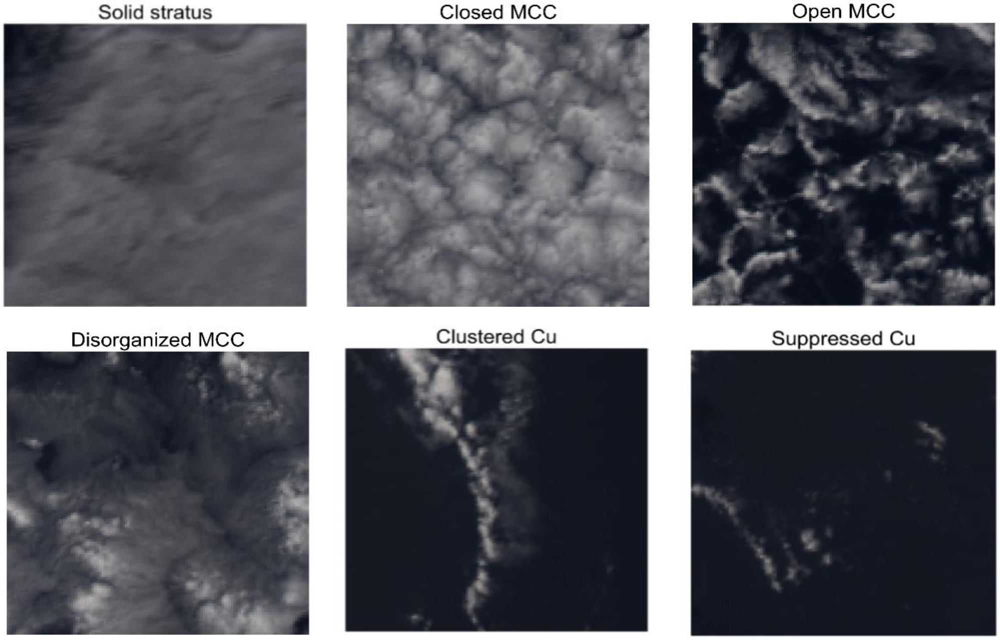

Figure 1: Example scenes of six cloud morphological types: solid stratus, closed mesoscale cellular convection, open mesoscale cellular convection, disorganized mesoscale cellular convection, clustered cumulus and suppressed cumulus. They are visible light images composed of channels 1, 4, 3 and the spatial resolution is 1° × 1°.

2.2 Data

The primary observation data utilized in this study were derived from the Moderate Resolution Imaging Spectroradiometer (MODIS) aboard NASA's Aqua satellite, including the Level-1B radiance product MYD021KM and the Level-2 cloud product MYD06 (Platnick et al., 2017), both with a spatial resolution of 1 km at nadir point. The thermal infrared radiance data from MYD021KM were used for model training and testing, while the cloud properties from MYD06 were utilized for quality control, low clouds filtering and statistical analyses. First, we selected daytime MODIS images over the Southeast Pacific (SEP) from January to June of 2014 to create our classification dataset. The representativeness of this dataset was validated as the probability density functions (PDFs) of thermal radiance data and cloud optical thickness show large overlap with those of the global and full-year dataset (Fig. S1). After dividing them into 128 × 128 pixels scenes, we filtered out the cloudless scenes (cloud fraction less than 1%) and scenes containing a large amount of high clouds or ice clouds (high/ice cloud exceeding 10%). High clouds are defined as those with cloud top height above 6km, ice clouds are those with cloud top temperature below 273.15K. In addition, the severe stretching at the edge of MODIS granules has been avoided by filtering scenes with sensor zenith angle greater than 45°. Ultimately, these eligible scenes are manually classified into one of the six categories. The cloud properties from MYD06 product, such as cloud top height (CTH), cloud liquid water path (CLWP), cloud optical thickness (COT) and cloud effective radius (CER) are used to help label and check the results with the cloud dataset (Mohrmann et al., 2021). A total of 38,756 labeled daytime scenes were obtained, including 3,548 scenes of solid stratus, 6,277 of closed MCC, 3,345 of open MCC, 6,739 of disorganized MCC, 8,947 of clustered Cu and 9,900 of suppressed Cu. These scenes were then randomly partitioned into three mutually independent datasets for training, validation, and testing, with a distribution ratio of 3:1:1 respectively. Despite the disparity in sample sizes across different types~~within our training dataset~~, ~~it~~our training dataset is capable of yielding superior model performance compared to a balanced dataset (Fig. S2).

In order to classify daytime and nighttime morphological types using one model only, we utilized daytime radiance data to train our model. Thermal infrared (TIR) channels 29 (8.7µm), 31 (10.8µm) and 32 (12.0µm) were specifically chosen as they most effectively represent the cloud properties and cloud-top temperature. Notably, owing to the subtle temperature variations on the cloud top, our model is unable to comprehensively discern convective cellular structures within the clouds by using radiance data only. Incorporating COT can better address the model's shortcomings in studying these cellular structures by providing cloud thickness information. Considering that there are no nighttime COT in the Level-2 cloud product MYD06, we used the COT data retrieved by Wang et al. (2022) as the fourth channel input for our model. Their all-day COT products, obtained using a thermal infrared CNN model, have shown a good consistency with both daytime products from MODIS and all-day products from active sensors. To validate the reliability of using TIR-CNN-based COT as a replacement for MODIS COT, we conducted a sensitivity experiment: comparing our classification with the outputs of a CNN trained on MODIS daytime COT. The results (Fig. S3) showed that the accuracy of both models is nearly identical, indicating that TIR-CNN-based COT is a reliable alternative to MODIS COT. In addition, we further examined the differences in the PDFs of the thermal radiance data and the TIR-CNN-based COT between our training dataset (daytime) and nighttime dataset. As depicted in Fig.

S4, these PDFs nearly overlapped, which means less extrapolation will be introduced when the model is generalized to nighttime data. And it also illustrates the credibility of our nighttime classification results. In summary, all the variables and datasets used in this study are outlined in Table 1.

Table 1 Summary of datasets used in the study.

Dataset	Count	Channels	Day/Night	Size	Period
Training dataset	23,254	29,31,32, COT	Daytime	128×128	January–June 2014
Validation dataset	7,751	29,31,32, COT	Daytime	128×128	January–June 2014
Testing dataset	7,751	29,31,32, COT	Daytime	128×128	January–June 2014
Application dataset	18 million	29,31,32, COT	Daytime and Nighttime	1°×1° (128×128)	2018–2022

Before starting training, we first converted the radiance data into Brightness Temperature (BT) according to the inverse Planck Function shown in Eq. (1):

$$\mathrm{BT}(\lambda, \mathrm{L}) = \frac{\mathrm{C}_2}{\lambda \ln(\mathrm{C}_1/\lambda^5 \mathrm{L}+1)} , (1)$$

where λ is the wavelength (μm), L represents the radiance ($\mathrm{W/m^2 \cdot sr \cdot \mu m}$), $\mathrm{C_1}=1.191042\times10^8(\mathrm{W/m^2 \cdot sr \cdot \mu m^{-4}})$, and $\mathrm{C_2}=1.4387752\times10^4$ (K·μm). We combined BT data from the three thermal infrared channels according to the Day and Night colour scheme proposed by Lensky and Rosenfeld (2008) (Table 2). Table 2 includes both the original Day and Night color scheme and our modified scheme used in this study. Different from the original Day and Night scheme, we did not clip each scene's data to a fixed range of maximum and minimum values. We think clipping might lead to the loss of important information, such as convective cell characteristics, which will affect model performance. In our scheme, the data of each scene may be compressed into different ranges and cause slight color variations in each scene image (Fig. 4), it has little impact on the model's judgment capability since the convolutional neural network primarily focuses on the statistical relationships between adjacent pixels in satellite images (Goodfellow, 2016). Moreover, after multiple rounds of practical training adjustments, we decided to use a factor of 2 to stretch the green channel to achieve a better model prediction outcome. To enhance the training efficiency and accuracy, the combined BT data and COT are normalized using Min-Max normalization following Eq. (2):

$$x_\mathrm{n} = \frac{x - min(x)}{max(x) - min(x)} , (2)$$

where x represents the input data, x_n represents the data after normalization, $\min(x)$ and $\max(x)$ represent the minimum and maximum values of the input data, respectively.

Table 2 The original (adapted from Lensky and Rosenfeld (2008)) and modified Day and Night color schemes

Color scheme	Red				Green				Blue			
	Channel	Min	Max	Stretch	Channel	Min	Max	Stretch	Channel	Min	Max	Stretch
Original Day and Night	IR12.0–IR10.8	−4 K	2 K	Linear	IR10.8–IR8.7	0 K	6 K	$\Gamma=1.2$	IR10.8	248K	303K	Linear
Modified Day and Night	IR12.0–IR10.8	min	max	Linear	IR10.8–IR8.7	min	max	$\Gamma=2$	IR10.8	min	max	Linear

To align with conventional climate datasets, we developed a standard 1° ×1° gridded datasets by applying the trained model to 1°-resolution images, where the 1° × 1° satellite images were interpolated and refined to 128 × 128 pixels.

For the purpose of investigating the influence of meteorological conditions on low-cloud morphologies, we conducted some statistical analyses utilizing the co-located hourly ERA5 reanalysis data (1° × 1°) from European Centre for Medium-Range Weather Forecasts (ECMWF). The co-location is achieved by spatially selecting the nearest ERA5 grid point to each MODIS observation and temporally interpolating the ERA5 data to match the exact time of the MODIS observations. This ensures accurate alignment between the two datasets in both space and time. Several variables, such as sea surface temperature (SST), relative humidity (RH), vertical velocity (ω) and divergence (1000 hPa, 700 hPa), can be directly obtained from the reanalysis data, while lower tropospheric stability (LTS) needs to be calculated using the following equation (3):

$$LTS = \theta_{700\mathrm{hPa}} - \theta_{1000\mathrm{hPa}}\ , (3)$$

where θ is the potential temperature.

Furthermore, we retrieved 5-year daytime and night-time CER (r_e) and COT (τ) using the TIR-CNN model from Wang et al. (2022) for subsequent statistical analysis for cloud properties. This approach will ensure the consistency of data range by using the same cloud detection algorithm. We can further calculate the liquid water path (LWP) utilizing Eq. (4):

$$\mathrm{LWP} = \frac{2}{3}\rho_w \tau r_e\ , (4)$$

with ρ_w the density of liquid water.

2.3 Marine Low-cloud Mesoscale Morphology Dataset

Our cloud dataset provides global classifications of daytime and nighttime marine low-cloud mesoscale morphology for the years 2018-2022, with a spatial resolution of 1° × 1° and a temporal resolution of 5 minutes. The dataset is provided in two kinds of files: those prefixed with "day" store the daytime classification results for each year, while files with the prefix "night" contain the nighttime classification results for each year. Both sets of files include the same variables. Table 3 provides an overview of the variables and their associated information. The key variables in the dataset include ‘date’ (representing the time of the 1° × 1° scene, formatted as the MODIS granule date), ‘lon’ and ‘lat’ (indicating the central longitude and latitude), and ‘cat’ (assigned cloud category, the values from 0 to 5 correspond to 'Solid Stratus', 'Closed MCC', 'Open MCC', 'Disorganized MCC', 'Clustered Cu', and 'Suppressed Cu', respectively). Additionally, ‘cert’ represents the model certainty, quantifying the probability that the cloud morphology belongs to the assigned category. ‘low_cf’ denotes the low cloud fraction, and ‘COT_CNN’, ‘CER_CNN’, and ‘LWP_CNN’ provide the in-cloud average cloud optical thickness, effective radius, and liquid water path respectively, as derived from the TIR-CNN model from Wang et al. (2022). The ‘Sensor_zenith’ variable indicates the scene average sensor zenith angle.

Table 3 Variables of the Daytime and Nighttime Global Marine Low-cloud Mesoscale Morphology Dataset

Variable Name	Description	Source	Spatial Resolution	Temporal Resolution	Units
date	Time of the 1°×1° grid point, formatted as 'YYYYDDD.HHHH'	MODIS MYD021	1° × 1°	5 minutes	-
lon	Central longitude (-180,180)	MODIS MYD021	1° × 1°	5 minutes	degree (°)
lat	Central latitude (-60,60)	MODIS MYD021	1° × 1°	5 minutes	degree (°)
cat	Category of the cloud morphology: 0-Solid stratus, 1-Closed MCC, 2-Open MCC, 3-Disorganized MCC, 4-Clustered Cu, 5-Suppressed Cu	Cloud Classification Model	1° × 1°	5 minutes	-
cert	Model certainty	Cloud Classification Model	1° × 1°	5 minutes	-
low_cf	Cloud fraction of low clouds	MODIS MYD06	1° × 1°	5 minutes	-
COT_CNN	In-cloud average cloud optical thickness (COT)	TIR-CNN model of Wang et al. (2022)	1° × 1°	5 minutes	-
CER_CNN	In-cloud average cloud effective radius (CER)	TIR-CNN model of Wang et al. (2022)	1° × 1°	5 minutes	µm
LWP_CNN	In-cloud average cloud liquid water path (LWP)	Calculated from COT_CNN and CER_CNN	1° × 1°	5 minutes	g/m^2
Sensor_zenith	Scene average sensor zenith angle	MODIS MYD021	1° × 1°	5 minutes	degree (°)

2.4 Method

In this study, a machine learning (ML) model ResNet-50 (Koonce, 2021) was chosen as our model architecture. It is a deep CNN model which employs a residual learning framework to construct a network with 50 convolutional layers. Despite a fairly deep convolutional layer, the incorporation of residual units in ResNet-50 enables direct signal transmission from earlier to later layers, ensuring high computational efficiency in deep architectures and markedly boosting both accuracy and the speed of convergence. We made some adjustments to the overall architecture of ResNet50 to better suit our datasets and the fine-tuned model structure is presented in Fig. 2a. The number of input channels was set to 4 to include the additional COT channel. Then, we configured the output dimension of the final fully connected layer to 6 to produce a probability distribution over the 6 output classes for each scene via a softmax activation function. The internal structure of ResNet50 remains unchanged, consisting of a preprocessing layer, four stages, and a global average pooling. The preprocessing layer includes a convolutional layer, a batch normalization (BN) layer, a ReLU activation function, and a Max Pooling layer. Each stage contains several residual blocks and is connected by skip connections (Fig. 2b).

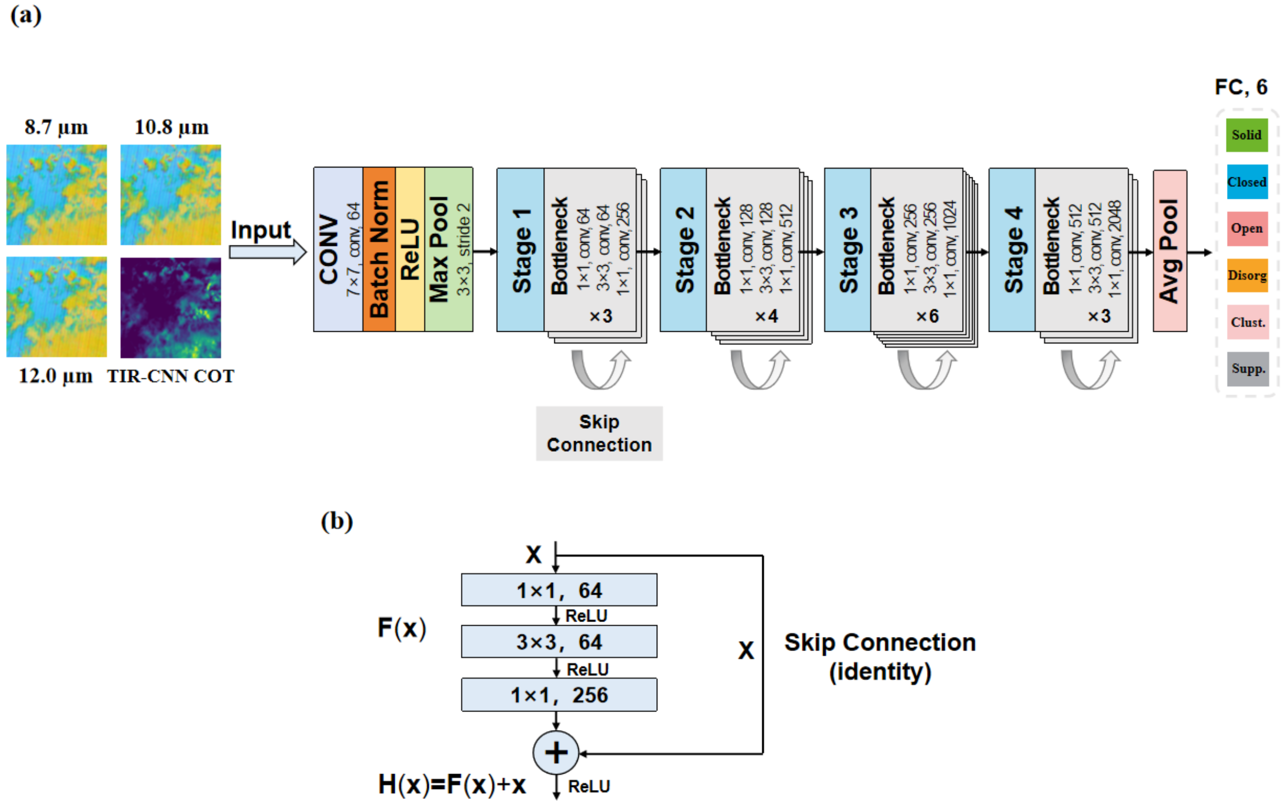

Figure 2: (a) The fine-tuned ResNet50 model architecture. (b) The skip connection structure of the residual blocks in the model.

Throughout the training process, we employed the Adaptive Moment Estimation (Adam) optimizer for gradient descent calculation and utilized cross-entropy as the loss function. Given the substantial size of our training dataset, we chose a batch size of 256 to enhance memory utilization and expedite the training process. In addition, to counteract the tendency for overfitting due to the increased noise in the radiance data of thermal infrared channels, we applied random rotation augmentation to the training images with a 50% probability. L2 regularization was also introduced to further decay the weights and prevent overfitting.

After each training epoch, the validation dataset was used to evaluate the trained model's performance, which allows us to monitor the model's success. When the training process was completed, the test dataset was used for the final evaluation of the model's performance. We used the optimal model to predict each sample in the test dataset, compared the model’s predictions with the true labels, and assessed the accuracy using metrics such as accuracy, F1-score, and recall.

3 Results

3.1 Model performance

In this section, our model performance is evaluated and a nighttime classification example is given. Our model begins to show signs of convergence around the 50th epoch, with its maximum validation accuracy reaching around 92% by the 65th epoch (Fig. S5). Compared to training without the incorporation of COT, the model's accuracy improved by 4%. Although it is a bit less accurate compared to the visible light model from Yuan et al. (2020), it is undeniable that this model has achieved a relatively high accuracy level when compared to other TIR model (Lang et al., 2022), and can effectively accomplish the classification tasks we proposed. The optimal model is subsequently evaluated on an independent test dataset, yielding the confusion matrix illustrated in Fig. 3. Elements on the diagonal represent the model's prediction accuracy for each type. Our model achieves an average precision of approximately 91%, an F1-score of 90.6%, and a recall of 90.8% on the test set, demonstrating its strong generalization capability and robustness.

Meanwhile, the confusion matrix (Fig. 3) shows that model's predictive performance varies across six cloud types, with higher accuracy for suppressed Cu and open MCC, but lower accuracy for disorganized MCC. Notably, this pattern is independent of sample size (Fig. S2) and is more likely due to confusion with other cloud types, as ~~In our model, closed MCC is more likely to be misidentified as solid stratus or disorganized MCC, while~~ disorganized MCC ~~tends to be~~clouds are frequently ~~misclassified~~ misidentified as clustered Cu or closed MCC (Fig. 3). ~~As observed in s~~Some classification samples~~,~~ reveal that such misclassifications are particularly common in ~~these misclassifications are partly attributed to the existence of~~ mixed and transitional scenes (Fig. S6), where the overlapping features of different cloud types often lead to ambiguity in model predictions. In addition, considering the similarity between the morphology of these clouds, the misclassifications may be related to the model's limited capacity to distinguish between stratiform structures and convective cells due to the small temperature difference on the cloud top. This can also be reflected in the sample images (Fig. S7).

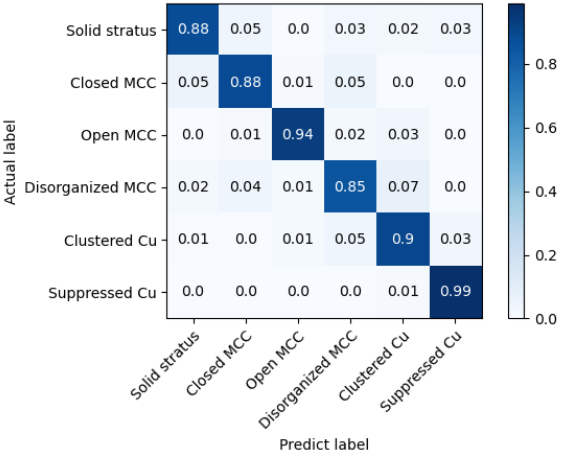

Actual label \ Predict label	Solid stratus	Closed MCC	Open MCC	Disorganized MCC	Clustered Cu	Suppressed Cu
Solid stratus	0.88	0.05	0.0	0.03	0.02	0.03
Closed MCC	0.05	0.88	0.01	0.05	0.0	0.0
Open MCC	0.0	0.01	0.94	0.02	0.03	0.0
Disorganized MCC	0.02	0.04	0.01	0.85	0.07	0.0
Clustered Cu	0.01	0.0	0.01	0.05	0.9	0.03
Suppressed Cu	0.0	0.0	0.0	0.0	0.01	0.99

Figure 3: The confusion matrix of the model's predictions on the test dataset. The rows of confusion matrix represent actual categories, columns represent predicted categories. The elements on the diagonal indicate the proportion of samples correctly classified by the model in each category.

Training by daytime infrared data, this model can be applied to nighttime scenarios, as shown in Fig. 4. Circles with different colors represent different cloud categories within the 1°×1° grid. Grids without circles indicate that they do not meet the criteria outlined in Section 2. The pseudo-RGB images are composed of thermal infrared channels 29, 31, 32 following the modified Day and Night color scheme (Table 2). This scheme provides a clearer visual distinction between different cloud types. However, as the data range for each image is not fixed, the colors of different cloud types will vary in different situations. For example, in the left granule image, light yellow represents low water clouds, green indicating thin cirrus and dark yellow signifying thick cumulonimbus clouds. In the sample scenes of open MCC and suppressed Cu, the yellow of low clouds becomes lighter and the green indicates small cumulus cloud. As for the remaining four cloud types, the surrounding thin cirrus appears in green while the stratiform clouds and shallow cumulus convections are both depicted in a brighter yellow due to their similar temperatures. Thus, it is challenging to discern convective cells among the yellow background of stratiform clouds. That is why we incorporated COT to assist in model predictions.

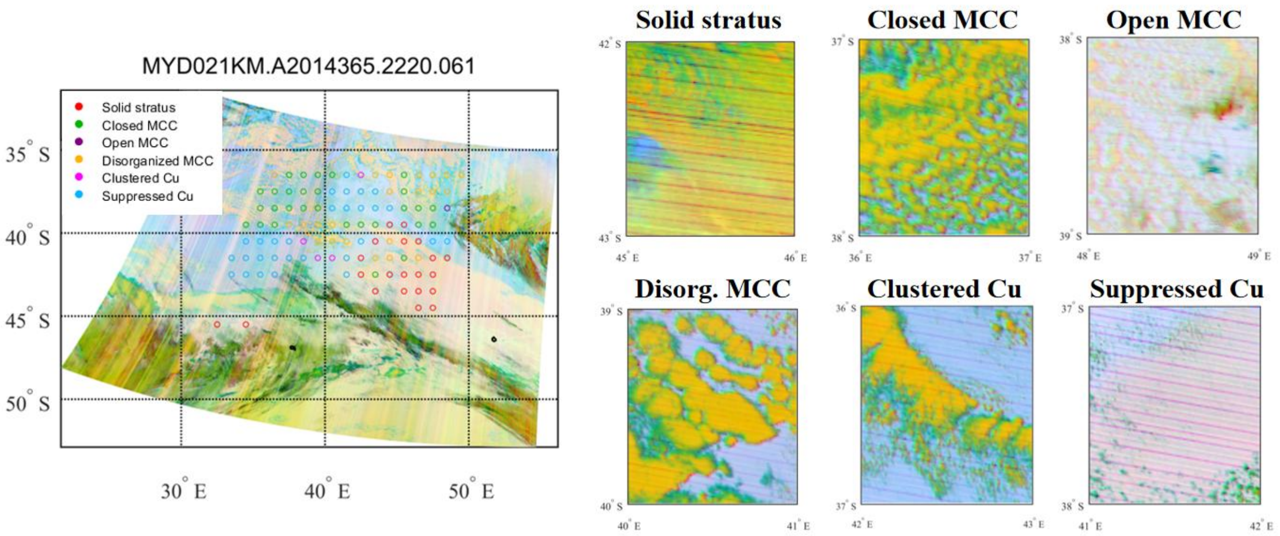

Figure 4: A nighttime classification example for MODIS image taken at 22:20 UTC on December 31, 2014. The pseudo-RGB images were generated from the combination of 29, 31, 32 thermal infrared channels while the classification results were derived by incorporating the retrieved Cloud Optical Thickness (COT) data.

3.2 Climatology of morphological types

Using the well-trained ResNet-50 model, we classified nearly 18 million 1° MODIS scenes and recorded the occurrence counts of different cloud types. The occurrence counts of each cloud type were divided by the total occurrences of the six cloud types within each grid to calculate their relative frequency of occurrence (RFO). The daytime climatology of RFO for the six cloud types is presented in Fig. 5. Each subplot's upper-right corner displays n and a percentage, with n denoting the total number of occurrences for each cloud type during the daytime over the five-year period, while the percentage indicates the proportion of each cloud type's five-year occurrences (n) relative to the five-year total occurrences of all six cloud types, which called total relative frequency.

Solid stratus predominantly distributes in nearly symmetrical latitude bands between 40°N–60°N and 50°S–60°S with a total relative frequency of 14%. In the mid to high latitudes of the Southern Hemisphere, its RFO exceeds 90%, which is higher than that in the Northern Hemisphere. Additionally, a substantial presence of solid stratus is also observed along the western coasts of continents in tropical and subtropical regions. Closed MCCs mainly appear in the cold eastern subtropical and mid-latitude oceans, with marked peak along the western coasts of the North America, South America and Africa. Their total relative frequency during the daytime is relatively low, accounting for only 5%. Disorganized MCCs exhibit a distribution pattern similar to closed MCC but are typically located farther offshore. They cover more extensive area and occur more frequently. The total relative frequency of disorganized MCC during the daytime is 15%, three times higher than closed MCC.

In addition, it is worth noting that, the peak areas of disorganized MCC appear in the west of closed MCC. This may be related to the transition between these two cloud types. The occurrence of open MCCs is least frequent over the global ocean, accounting for only 3%. In the water areas west of Peru, there is a minor frequency peak of open MCC, which may be attribute to the fragmentation of closed MCC caused by strong winds and precipitation (Rosenfeld et al., 2006; Eastman et al., 2022). Clustered Cu and suppressed Cu are primarily observed in tropical and subtropical regions. They have the highest overall relative frequencies, both around 30%. However, in terms of their spatial distribution, clustered cumulus is more prevalent over central and western oceans, while suppressed Cu commonly peaks in coastal waters near continents. We have compared the daytime climatology with the results from Yuan et al. (2020) using visible light channels and consistent results are obtained (Fig. S8).

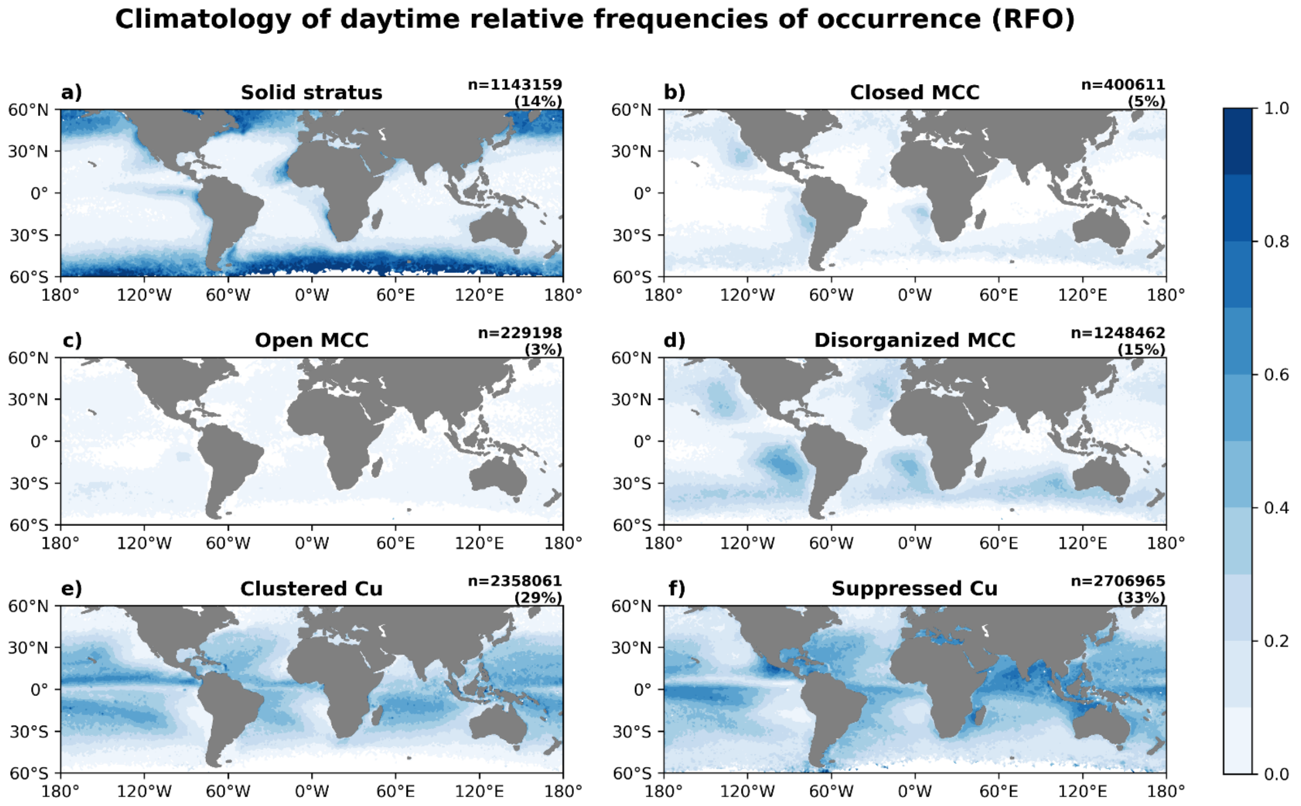

Figure 5: The climatology of daytime relative frequencies of occurrence (RFO) for six categories from 2018 to 2022. N represents the total number of occurrences for each cloud type during the day over the five-year period, while the percentage indicates the proportion of each cloud type's five-year occurrences relative to the five-year total occurrences of all six cloud types.

In Fig. 6, the spatial distribution of these six cloud types remains largely unchanged at night, but their RFO show notable variations. Figure 7 presents the nighttime–daytime contrast in RFO for each morphological type (nighttime minus daytime).

The total nocturnal frequency of solid stratus clouds is 15%, which is similar to daytime. At night, they occur more frequently over mid-latitude oceans and less frequently in low-latitude regions. The RFO for closed MCC shows a pronounced increase at night, reaching approximately twice the levels of the daytime. Some of the increase occurs over mid-latitude oceans, while the most significant rise is observed over the eastern subtropical ocean, particularly in the Southern Hemisphere (Fig. 7). The overall frequency of open MCC remains relatively unchanged at night, while the total frequency of disorganized MCC and clustered Cu slightly increase. At nighttime, the RFO of all these three cloud types decrease over the colder eastern subtropical and mid-latitude oceans, while increase over the warmer sea surface at lower latitudes (Fig. 7). Notably, westward from the continents, the night-time frequency pattern of disorganized MCC exhibits an initial decrease followed by an increase. This opposite trend is most pronounced along the western coast of South America. Among six cloud types, only the total frequency of suppressed Cu experiences a marked decline at night, with a total decrease of 11%. A statistical analysis of some meteorological conditions will be conducted in Section 3.5. Exploration of the critical cloud-controlling factors contributing to these diurnal variations will be done in the future.

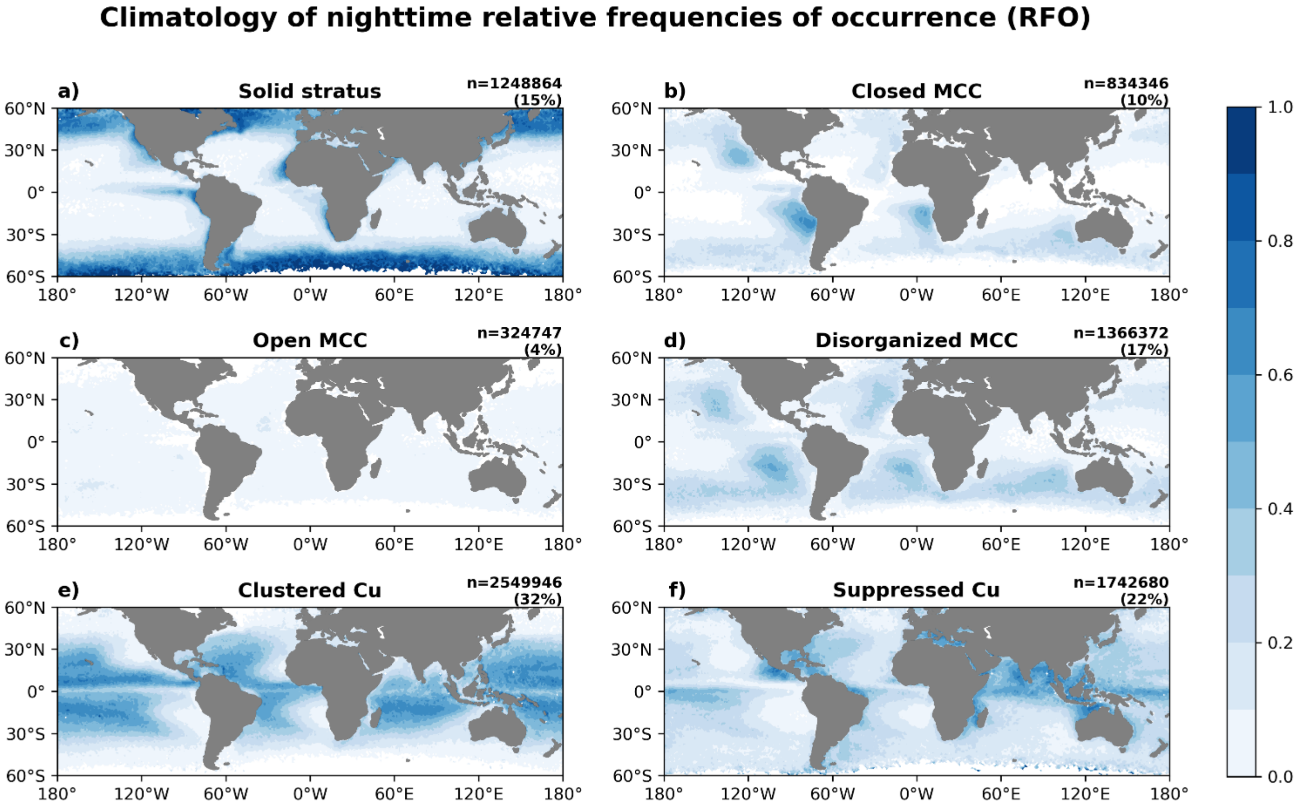

Figure 6: The climatology of nighttime relative frequencies of occurrence (RFO) for six categories from 2018 to 2022.

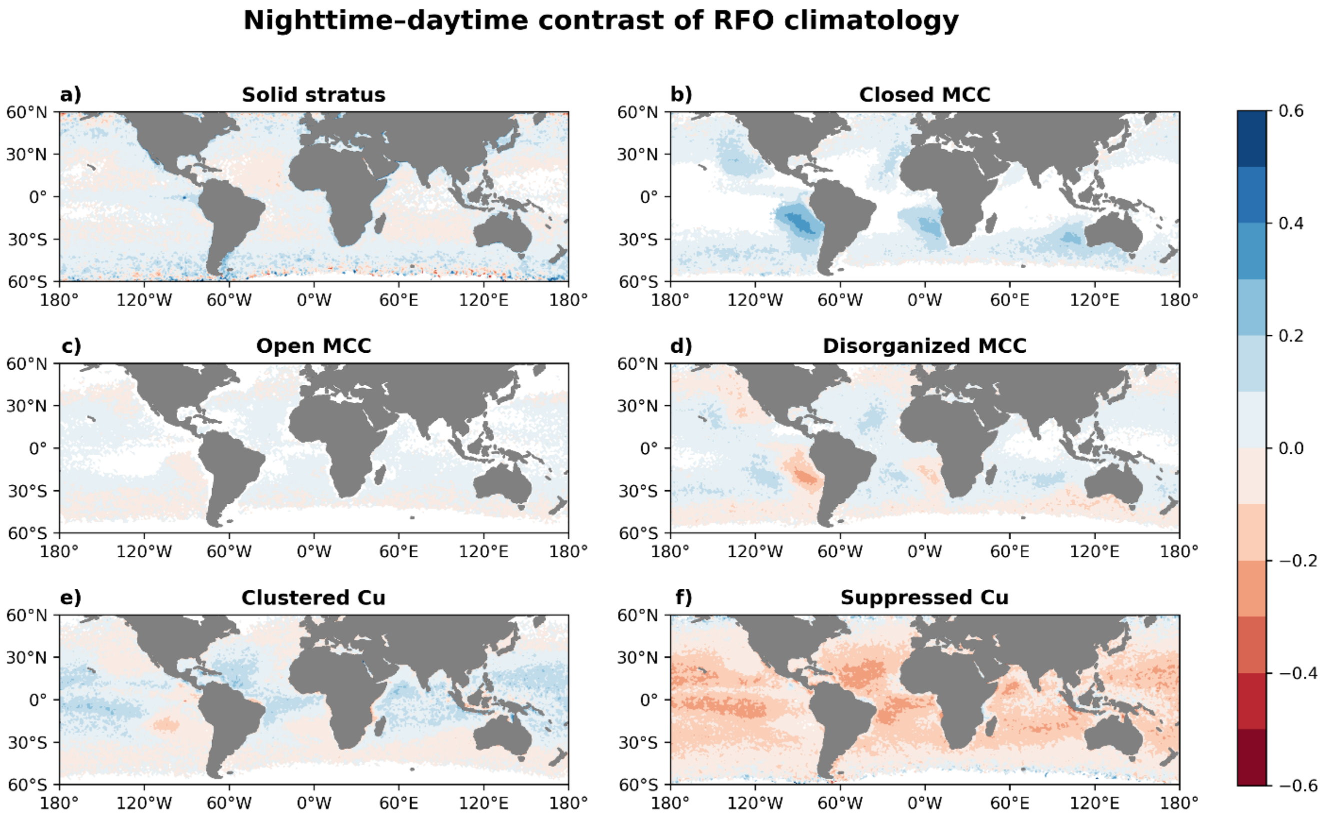

Figure 7: The difference between daytime and night-time RFO for each morphological type (nighttime minus daytime).

3.3 Seasonal variations in morphological types

We further classified the RFO of different cloud morphologies by season. Figure 8 presents the seasonal variation of daytime RFO while Fig. 9 shows the nighttime situation. It can be seen from the two figures that the RFO of these six cloud types exhibit similar seasonality in both day and night. At mid latitudes, solid stratus clouds usually peak during the summer of the respective hemisphere (JJA for the Northern Hemisphere, DJF for the Southern Hemisphere) and have the lowest occurrence during the winter (DJF for the Northern Hemisphere, JJA for the Southern Hemisphere). They show equal RFO during spring and autumn in both hemispheres (MAM and SON). The peak occurrence of solid stratus in mid-latitude regions aligns with the latitudinal shift of solar insolation. Thus it can be inferred that the increased temperature and enhanced moisture available from melted sea ice may contribute to the peak in summer (Herman and Goody, 1976). The RFO of closed MCC notably increases during the winter (JJA) and spring (SON) in the Southern Hemisphere, particularly in the southeast Pacific (SEP) and southeast Atlantic (SEA) regions. McCoy et al. (2017) suggest that the seasonal cycle of closed MCC in such regions correlates well with estimated inversion strength (EIS). In contrast to solid stratus, open MCC demonstrates an opposite seasonal cycle in mid-latitudes, with the highest frequency occurring in the winter of respective hemisphere (DJF for the Northern Hemisphere and JJA for the Southern Hemisphere). Previous work suggests that its seasonality is more likely associated with cold air outbreaks in mid-latitude oceanic regions (McCoy et al., 2017). This may also explain why open MCC exhibits zonal frequency peak over the Southern Pacific during the winter of Southern Hemisphere (JJA) (Fig. 8 and Fig. 9). Disorganized MCC clouds occur more frequently over warmer ocean surface western of the continents during the summer of respective hemisphere (JJA in the Northern Hemisphere and DJF in the Southern Hemisphere) and occur less frequently during the winter of respective hemisphere (DJF in the Northern Hemisphere and JJA in the Southern Hemisphere). Thus, the sea surface temperature may be one of the controlling factors of its seasonal variation. All the MCC types show distinct seasonal cycles while the clustered Cu and suppressed Cu do not show marked seasonal variations during both day and night.

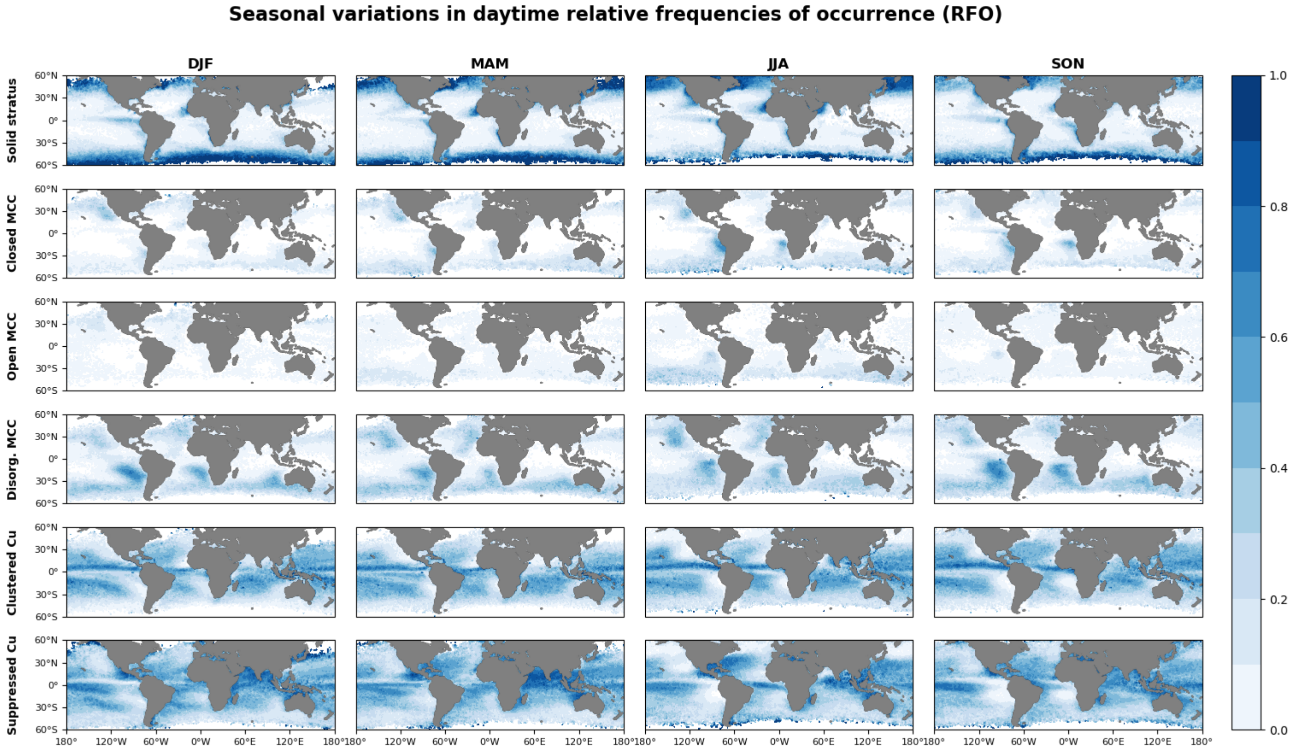

Figure 8: Seasonal variations of daytime relative frequencies of occurrence (RFO).

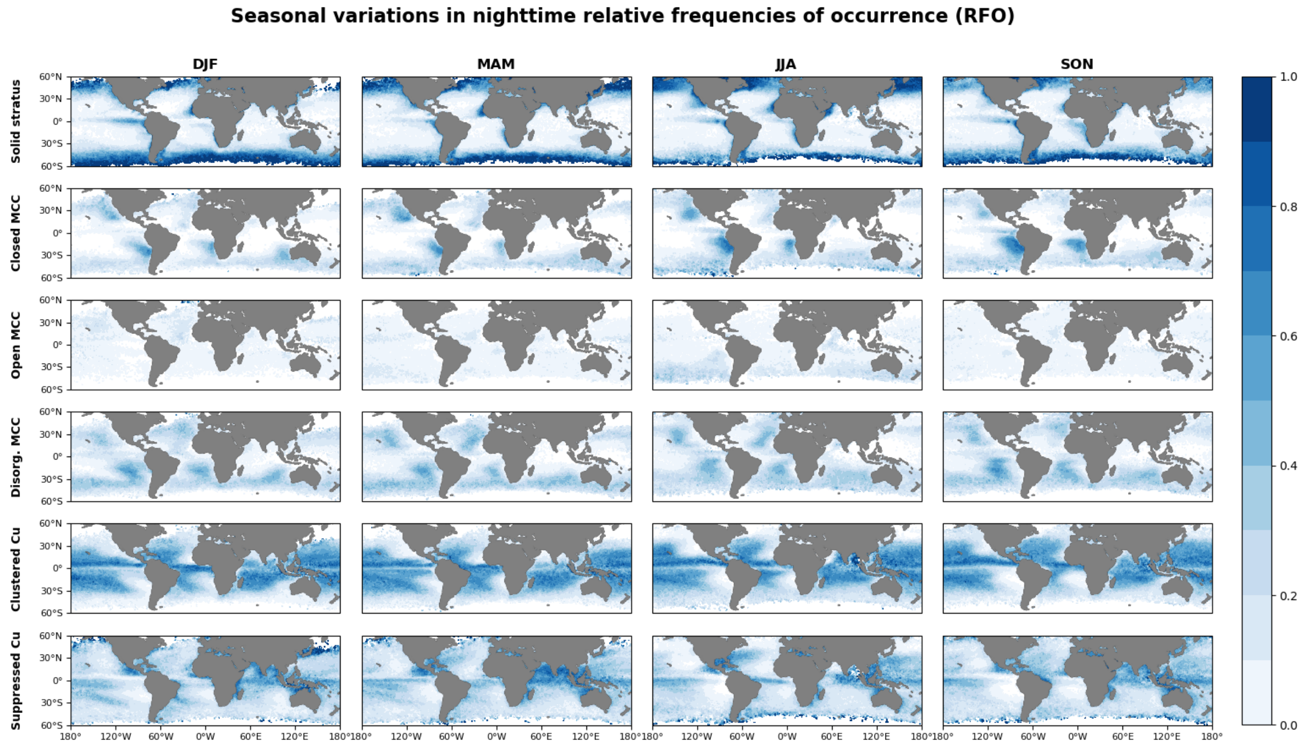

Figure 9: Seasonal variations of nighttime relative frequencies of occurrence (RFO).

3.4 Cloud properties

Different clouds types exhibit different radiative effects due to their unique physical characteristics. In Fig. 10, we compared the physical properties of each cloud type in both day and night, including cloud fraction (CF), cloud effective radius (CER), cloud liquid water path (LWP), and cloud optical thickness (COT). The CF is derived from the cloud mask in the Level-2 cloud product MYD06, while CER and COT are both retrieved using the method from Wang et al. (2022). LWP is calculated from CER and COT as mentioned in Section 2.2. All of the cloud microphysical properties represent the in-cloud mean value within a 1°×1° grid.

Solid stratus and closed MCC possess the highest CF, therefore the increase in their nocturnal frequency may account for a major portion of the overall rise in cloud cover. Open MCC possesses the largest CER and it will decrease by 2 microns on average at night. In the daytime, closed MCC clouds exhibit the highest values of LWP and COT. At nighttime, their CER, LWP and COT increase further substantially, with a substantial magnitude. The four cloud properties of disorganized MCC also show a slight increase at nighttime.

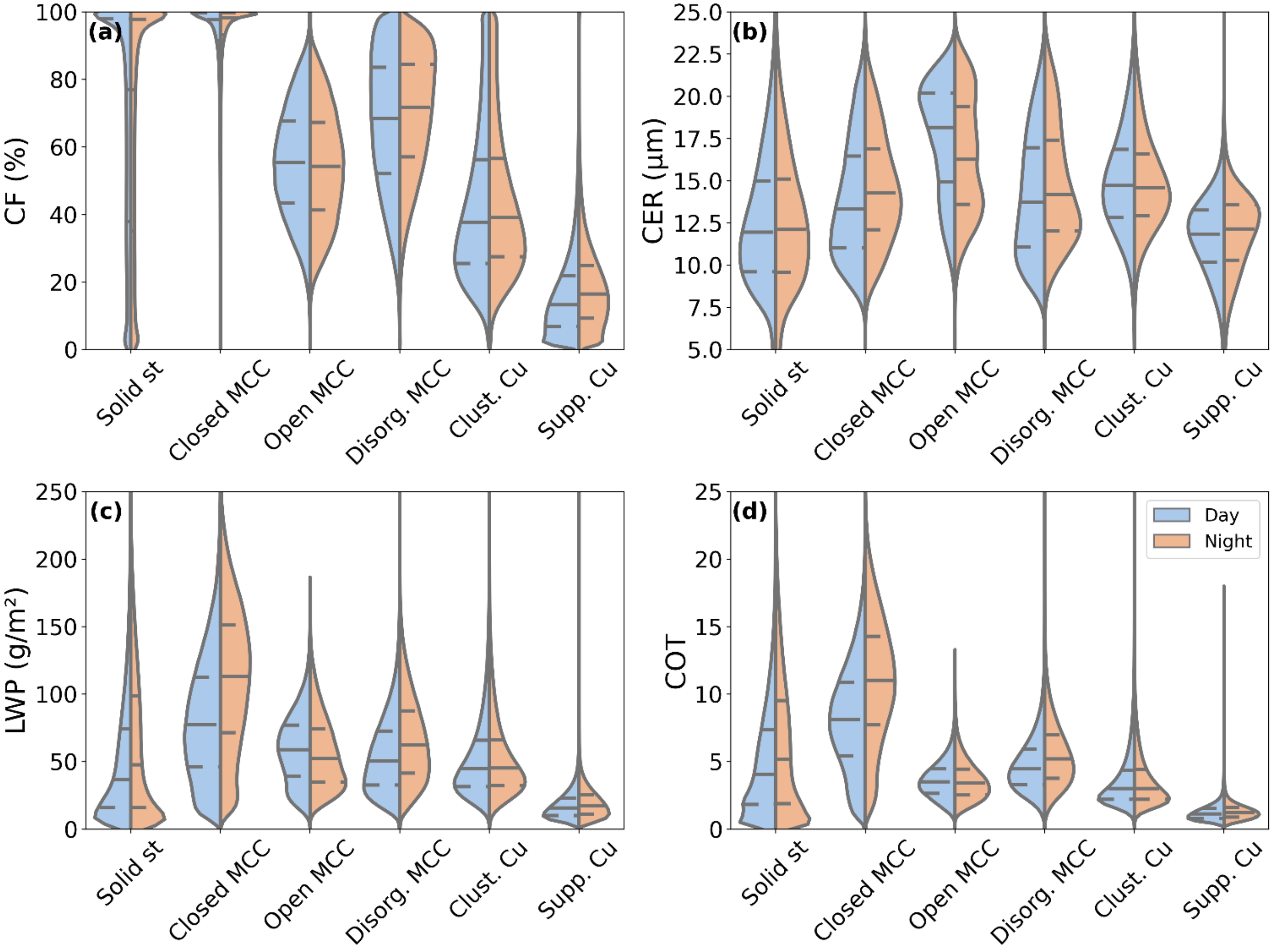

Figure 10: A violin plot of the properties of six cloud types over the global oceans from 2018 to 2022. (a) cloud fraction, (b) retrieved cloud effective radius, (c) cloud liquid water path, (d) retrieved cloud optical thickness. Blue represents the daytime data and yellow represents the nighttime data. The central long dashed line in each plot represents the median of the distribution, and the short dashed line indicates the interquartile range. The shape of the violin plots suggests the density distribution of the values, with wider sections indicating a higher frequency of data points.

3.5 Large-scale meteorological condition

The statistics of several meteorological factors which may control the marine low cloud morphology in the Southeast Pacific (SEP) region (0 – 30°S, 80°W – 120°W) are shown in Figure 11. The lower tropospheric stability (LTS) for the six cloud types is shown in Figure 11a. A higher LTS indicates a more stable lower troposphere. Closed MCC have the highest LTS, implying the significance of tropospheric stability in their formation. The two cumulus types have the lowest LTS because an unstable troposphere is conducive to cumulus activity. The LTS of six cloud types show different degrees of decline at nighttime, which may be due to the shift in their geographical locations. Sea surface temperature (SST) is the lowest for closed MCC during both day and night (Fig. 11b). Open MCC and disorganized MCC exhibit higher SST compared with closed MCC, which corresponds to their geographical positions. Two cumulus types have the highest SST. At nighttime, the increase of SST for different cloud types may also be attributed to their movements. Figure 11c and 11d show the relative humidity (RH) at 700hPa and 1000hPa respectively. Throughout the day and night, solid stratus clouds exhibit the highest RH at both 700hPa and 1000hPa. At the 700hPa level (Fig. 11c), the RH values for two cumulus types are higher than those for MCC clouds, while at the 1000hPa level (Fig. 11d), the difference is minimal. At night and at 700 hPa, the RH of solid stratus and two cumulus types increases, while that of closed MCC decreases. Due to lower temperatures at nighttime, the RH over sea surface for all six cloud types increases by a similar magnitude. Figure 11e indicates that all cloud types are associated with large-scale subsidence. Open MCC experiences the strongest upper-level subsidence, while solid stratus has the weakest vertical motion. At nighttime, the subsidence for all six cloud types weakens and closed MCC exhibits a more pronounced reduction. Figure 11f presents the boundary layer anomaly divergence which is calculated by subtracting the divergence at 700 hPa from the surface divergence. This index has been proven effective in distinguishing between the two cumulus types (Mohrmann et al., 2021). Suppressed Cu shows the largest boundary layer anomaly divergence, indicating that strong surface divergence favors the maintenance of suppressed Cu. Clustered Cu has the smallest anomaly divergence, with weaker surface divergence. Therefore, the weakening of surface divergence at nighttime may be the reason for the reduction of suppressed Cu.

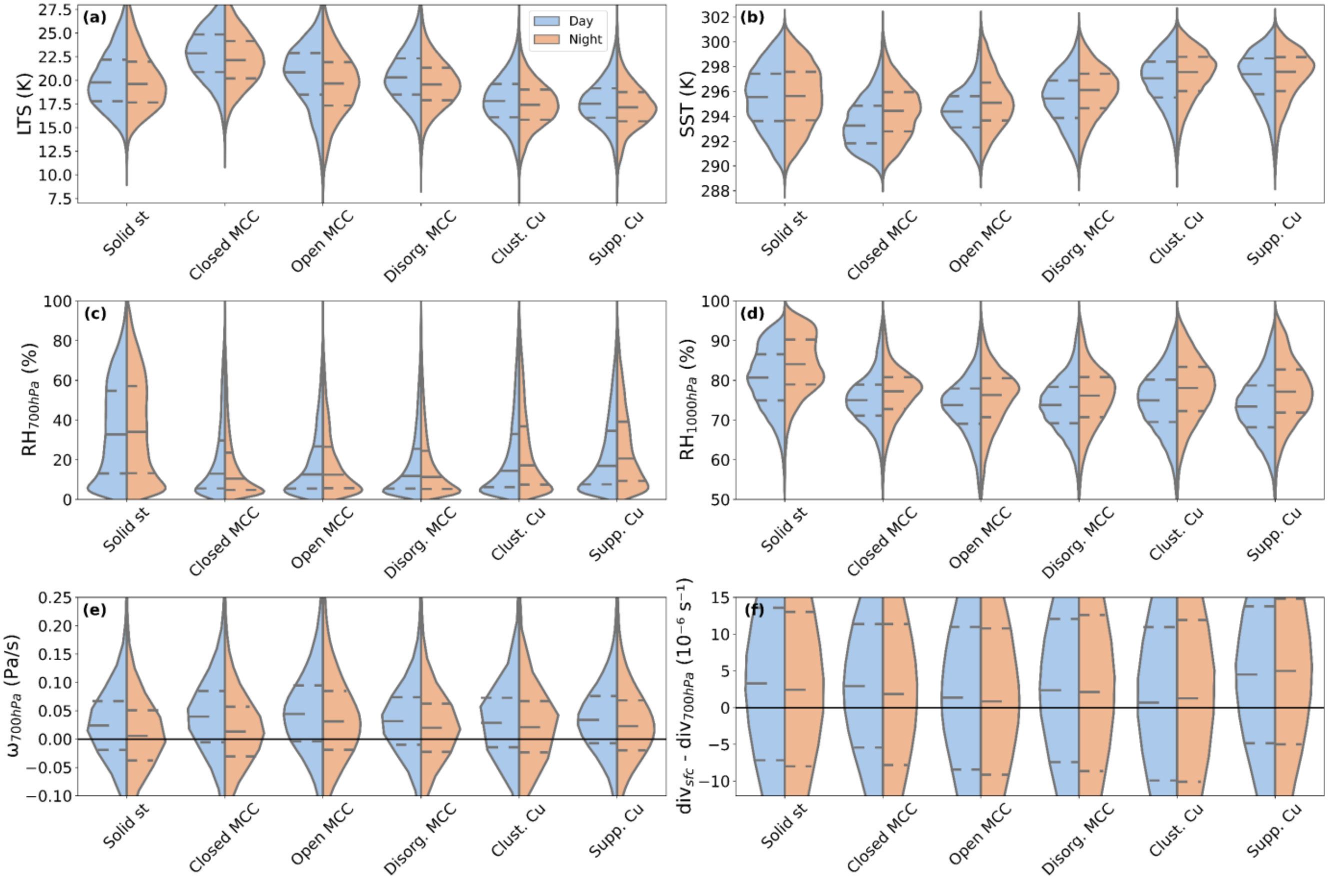

Figure 11: Same as Fig. 10, but shows day-night comparison of meteorological conditions in the Southeast Pacific (SEP) region (0–30°S, 80°W–120°W) from 2018 to 2022. All matched from ERA5 reanalysis data. (a) Lower tropospheric stability, (b) sea surface temperature, (c) 700hPa relative humidity, (d) 1000hPa relative humidity, (e) 700hPa vertical velocity, (f) boundary layer anomaly divergence.

4 Discussion

The mesoscale cloud morphology dataset presented in this paper enables a comparative investigation of cloud morphology during both daytime and nighttime. Its 1° × 1° resolution allows a better alignment with other gridded datasets, facilitating further studies on driving factors, precipitation efficiency, and radiative effects (shortwave and longwave).

Although our model has achieved a high prediction accuracy and performed well in the classification tasks, there is still room for improvement. In future work, the current CNN model ~~can~~ might be ~~considered~~ replaced with more advanced architectures and the quality of our training dataset ~~need to~~could be further improved. For the former one, novel deep CNN models can be applied to cloud morphology classification through transfer learning. For ~~example~~instance, the Xception model, which achieved an accuracy of 97.66% in classifying traditional cloud types (Guzel et al., 2024), could be considered. For the latter goal, removing the mixed and mislabelled scenes from ~~the~~ our training dataset, along with adding more global and multi-seasonal scenes will improve the model performance in identifying these cloud morphological types. Furthermore, ~~The~~ the limitations of brightness temperature in capturing cloud-top morphology significantly constrain the model's accuracy, which largely explains the performance gap between our nighttime model and the daytime model proposed by Yuan et al. (2020). Nevertheless, a 4% improvement in model accuracy achieved by incorporating COT indicates that integrating additional cloud property channels represent a promising avenue for further enhancing the performance of our model.

As we apply the model trained on 128 × 128 pixels scenes to the interpolated 1° × 1° cloud scenes, the issue regarding to scene area require further discussion. For a given latitude, when the satellite zenith angle changes, the area of 128 × 128 pixel will vary due to the pixel stretching, while the area of the 1° grid remains constant. This is an advantage of the 1° × 1° grid dataset as a larger the area has a larger possibility to cover multiple cloud types in one scene. However, at the same satellite zenith angle, the size of 1°× 1° grid will change with latitude, whereas the 128 × 128 pixel scene area remains undistorted, which is a limitation of the 1° × 1° grid dataset. Moreover, in some cases, especially with stratocumulus and cumulus clouds, interpolating images into a 1°× 1° grid may smooth or blur small-scale cloud features and introduce unrealistic structures that do not exist in the original images, which could lead to potential misclassifications of the model. Therefore, testing the model on a labeled, standard-grid dataset will be necessary in future work.

The six cloud types examined in this study are the most common and representative types over the ocean. However, they are not exhaustive. In future work, we will explore ~~the~~ all~~overall~~ low-cloud morphological types over the global land and ocean, and gradually extend to mid- and high-level clouds.

5 Data Availability

The ~~Daytime~~ daytime and nighttime cloud classification datasets, along with~~as well as~~ the model development datasets (training, validation, and test sets),~~our training dataset~~ are accessible on https://doi.org/10.5281/zenodo.13801408~~the https://doi.org/10.5281/zenodo.13801408~~ (Wu et al., 2024). The model and the code related to this article are available at https://github.com/YuanyuanWu-NJU/Cloud-morphology-dataset. MODIS data can be downloaded from NASA Official Website (https://ladsweb.modaps.eosdis.nasa.gov/). ERA5 reanalysis data are provided by ECMWF (https://cds.climate.copernicus.eu/datasets). The cloud property retrieval model of Wang et al. (2022) can be found at (https://github.com/WgQuan/cloud-property-retrievals).

6 Conclusion

In this study, approximately 40,000 MODIS daytime low-cloud scenes were manually labeled to train a deep residual network model, ResNet50. By using this model, we developed a new global standard-grid classification dataset (2018–2022) of marine low-cloud mesoscale morphology, encompassing classifications for both daytime and nighttime. Compared to the 128 × 128 pixel dataset of Yuan et al. (2020) and Mohrmann et al. (2021), our standard-grid dataset offers more uniform and widely applicable cloud morphology data, and more importantly, extending the dataset to nighttime. This dataset can integrate more easily with other climate and surface datasets, thus will provide a solid data foundation for future research on understanding cloud dynamics and their impact on climate.

The climatology of cloud morphologies is also analyzed. The results reveal that solid stratus dominates within the 50°–60° latitude bands and that closed MCC is most commonly found in the cold eastern subtropical and mid-latitude oceans. Disorganized MCC occurs on the warmer ocean surfaces west of closed MCC, with a much higher frequency. Open MCC is more evenly distributed across the global oceans but with the lowest frequency. In regions with higher sea surface temperatures, such as the tropics and the trade wind zone, clustered Cu and suppressed Cu are the primary types of marine low clouds. Clustered Cu is more prevalent over oceans and suppressed Cu is more concentrated along continental coasts.

When comparing the daytime and nighttime climatology, we found that there is a pronounced increase in the RFO of closed MCC during night, whereas the occurrence of suppressed Cu undergoes a significant decline. The frequencies of disorganized MCC and clustered Cu exhibit minor variation between day and night. From the perspective of different seasons, solid stratus and all MCC types exhibit clear seasonal cycles while two cumulus types do not show notable seasonality.

Although we have statistically analyzed the meteorological factors that may affect low cloud morphology, identifying the specific dominant factors for each cloud type remains challenging. In the context of global warming, the long-term trends of these cloud types during daytime and nighttime may also exhibit significant differences. The changes in Earth's radiation budget caused by low-cloud morphology transitions may have a substantial impact on climate sensitivity, which will be a topic of our future research.

Acknowledgments

This work is supported by the National Nature Science Foundation of China (42475089, 41925023, 42075093, U2342223, and 91744208).

Author contributions

Y.Z. designed the study, Y.W., J.L., Y.C., Y.Z. and D.R. wrote and revised the manuscript. J.L., Y.L., Y.C. and Q.W. collected the data. J.L. and Y.Z. contributed to the modeling and data process. Q.W. and C.Z. provided the cloud property retrieval model and Y.W. retrieved the cloud property product. K.H., B.Z., Y.W., Y.L. and C.Z. contributed to interpreting results and discussions. The entire study was conducted under the supervision of Y.Z., M.W., J.S. and D.R.

Competing interests

The authors declare no competing interests.

References

Bony, S., Schulz, H., Vial, J., and Stevens, B.: Sugar, Gravel, Fish, and Flowers: Dependence of Mesoscale Patterns of Trade-Wind Clouds on Environmental Conditions, Geophysical Research Letters, 47, e2019GL085988, https://doi.org/10.1029/2019GL085988, 2020.

Bretherton, C. S., McCoy, I. L., Mohrmann, J., Wood, R., Ghate, V., Gettelman, A., Bardeen, C. G., Albrecht, B. A., and Zuidema, P.: Cloud, Aerosol, and Boundary Layer Structure across the Northeast Pacific Stratocumulus–Cumulus Transition as Observed during CSET, Monthly Weather Review, 147, 2083-2103, https://doi.org/10.1175/MWR-D-18-0281.1, 2019.

Cao, Y., Zhu, Y., Wang, M., Rosenfeld, D., Zhou, C., Liu, J., Liang, Y., Huang, K.-E., Wang, Q., Bai, H., Wang, Y., Wang, H., and Zhang, H.: Improving Prediction of Marine Low Clouds Using Cloud Droplet Number Concentration in a Convolutional Neural Network, Journal of Geophysical Research: Machine Learning and Computation, 1, e2024JH000355, https://doi.org/10.1029/2024JH000355, 2024.

Cox, D. T. C., Maclean, I. M. D., Gardner, A. S., and Gaston, K. J.: Global variation in diurnal asymmetry in temperature, cloud cover, specific humidity and precipitation and its association with leaf area index, Global Change Biology, 26, 7099-7111, https://doi.org/10.1111/gcb.15336, 2020.

Dai, A.: Global Precipitation and Thunderstorm Frequencies. Part II: Diurnal Variations, Journal of Climate, 14, 1112-1128, https://doi.org/10.1175/1520-0442(2001)014<1112:GPATFP>2.0.CO;2, 2001.

Dai, A., Lin, X., and Hsu, K.-L.: The frequency, intensity, and diurnal cycle of precipitation in surface and satellite observations over low- and mid-latitudes, Climate Dynamics, 29, 727-744, https://doi.org/10.1007/s00382-007-0260-y, 2007.

Dai, A., Trenberth, K. E., and Karl, T. R.: Effects of Clouds, Soil Moisture, Precipitation, and Water Vapor on Diurnal Temperature Range, Journal of Climate, 12, 2451-2473, https://doi.org/10.1175/1520-0442(1999)012<2451:EOCSMP>2.0.CO;2, 1999.

Davy, R., Esau, I., Chernokulsky, A., Outten, S., and Zilitinkevich, S.: Diurnal asymmetry to the observed global warming, International Journal of Climatology, 37, 79-93, https://doi.org/10.1002/joc.4688, 2017.

Eastman, R., McCoy, I. L., and Wood, R.: Wind, Rain, and the Closed to Open Cell Transition in Subtropical Marine Stratocumulus, Journal of Geophysical Research: Atmospheres, 127, e2022JD036795, https://doi.org/10.1029/2022JD036795, 2022.

Eytan, E., Koren, I., Altaratz, O., Kostinski, A. B., and Ronen, A.: Longwave radiative effect of the cloud twilight zone, Nature Geoscience, 13, 669-673, https://doi.org/10.1038/s41561-020-0636-8, 2020.

Feingold, G., Koren, I., Wang, H., Xue, H., and Brewer, W. A.: Precipitation-generated oscillations in open cellular cloud fields, Nature, 466, 849-852, https://doi.org/10.1038/nature09314, 2010.

Goodfellow, I.: Deep Learning, MIT Press2016.

Goren, T., Kazil, J., Hoffmann, F., Yamaguchi, T., and Feingold, G.: Anthropogenic Air Pollution Delays Marine Stratocumulus Breakup to Open Cells, Geophysical Research Letters, 46, 14135-14144, https://doi.org/10.1029/2019GL085412, 2019.

Guzel, M., Kalkan, M., Bostanci, E., Acici, K., and Asuroglu, T.: Cloud type classification using deep learning with cloud images, PeerJ Computer Science, 10, e1779, https://doi.org/10.7717/peerj-cs.1779, 2024.

Herman, G. and Goody, R.: Formation and Persistence of Summertime Arctic Stratus Clouds, Journal of Atmospheric Sciences, 33, 1537-1553, https://doi.org/10.1175/1520-0469(1976)033<1537:FAPOSA>2.0.CO;2, 1976.

Klein, S. A. and Hartmann, D. L.: The Seasonal Cycle of Low Stratiform Clouds, Journal of Climate, 6, 1587-1606, https://doi.org/10.1175/1520-0442(1993)006<1587:TSCOLS>2.0.CO;2, 1993.

Koonce, B.: ResNet 50, in: Convolutional Neural Networks with Swift for Tensorflow: Image Recognition and Dataset Categorization, Apress, Berkeley, CA, 63-72, https://doi.org/10.1007/978-1-4842-6168-2_6, 2021.

Lang, F., Ackermann, L., Huang, Y., Truong, S. C. H., Siems, S. T., and Manton, M. J.: A climatology of open and closed mesoscale cellular convection over the Southern Ocean derived from Himawari-8 observations, Atmos. Chem. Phys., 22, 2135-2152, https://doi.org/10.5194/acp-22-2135-2022, 2022.

Lensky, I. M. and Rosenfeld, D.: Clouds-Aerosols-Precipitation Satellite Analysis Tool (CAPSAT), Atmos. Chem. Phys., 8, 6739-6753, https://doi.org/10.5194/acp-8-6739-2008, 2008.

Li, X., Qiu, B., Cao, G., Wu, C., and Zhang, L.: A Novel Method for Ground-Based Cloud Image Classification Using Transformer, Remote Sensing, 14, 3978, https://doi.org/10.3390/rs14163978, 2022.

Liu, J., Zhu, Y., Wang, M., and Rosenfeld, D.: Cloud Susceptibility to Aerosols: Comparing Cloud-Appearance vs. Cloud-Controlling Factors Regimes, EGU General Assembly 2024, Vienna, Austria, 14–19 Apr 2024, EGU24-4059, https://doi.org/10.5194/egusphere-egu24-4059, 2024.

Luo, H., Quaas, J., and Han, Y.: Diurnally asymmetric cloud cover trends amplify greenhouse warming, Science Advances, 10, eado5179, https://doi.org/10.1126/sciadv.ado5179, 2024.

McCoy, I. L., Wood, R., and Fletcher, J. K.: Identifying Meteorological Controls on Open and Closed Mesoscale Cellular Convection Associated with Marine Cold Air Outbreaks, Journal of Geophysical Research: Atmospheres, 122, 11,678-611,702, https://doi.org/10.1002/2017JD027031, 2017.

McCoy, I. L., McCoy, D. T., Wood, R., Zuidema, P., and Bender, F. A.-M.: The Role of Mesoscale Cloud Morphology in the Shortwave Cloud Feedback, Geophysical Research Letters, 50, e2022GL101042, https://doi.org/10.1029/2022GL101042, 2023.

Mohrmann, J., Wood, R., Yuan, T., Song, H., Eastman, R., and Oreopoulos, L.: Identifying meteorological influences on marine low-cloud mesoscale morphology using satellite classifications, Atmos. Chem. Phys., 21, 9629-9642, https://doi.org/10.5194/acp-21-9629-2021, 2021.

Muhlbauer, A., McCoy, I. L., and Wood, R.: Climatology of stratocumulus cloud morphologies: microphysical properties and radiative effects, Atmos. Chem. Phys., 14, 6695-6716, https://doi.org/10.5194/acp-14-6695-2014, 2014.

Petters, M. D., Snider, J. R., Stevens, B., Vali, G., Faloona, I., and Russell, L. M.: Accumulation mode aerosol, pockets of open cells, and particle nucleation in the remote subtropical Pacific marine boundary layer, Journal of Geophysical Research: Atmospheres, 111, https://doi.org/10.1029/2004JD005694, 2006.

Platnick, S., Meyer, K. G., King, M. D., Wind, G., Amarasinghe, N., Marchant, B., Arnold, G. T., Zhang, Z., Hubanks, P. A., Holz, R. E., Yang, P., Ridgway, W. L., and Riedi, J.: The MODIS Cloud Optical and Microphysical Products: Collection 6 Updates and Examples From Terra and Aqua, IEEE Transactions on Geoscience and Remote Sensing, 55, 502-525, https://doi.org/10.1109/TGRS.2016.2610522, 2017.

Rosenfeld, D., Kaufman, Y. J., and Koren, I.: Switching cloud cover and dynamical regimes from open to closed Benard cells in response to the suppression of precipitation by aerosols, Atmos. Chem. Phys., 6, 2503-2511, https://doi.org/10.5194/acp-6-2503-2006, 2006.

Savic-Jovcic, V. and Stevens, B.: The Structure and Mesoscale Organization of Precipitating Stratocumulus, Journal of the Atmospheric Sciences, 65, 1587-1605, https://doi.org/10.1175/2007JAS2456.1, 2008.

Schulz, H., Eastman, R., and Stevens, B.: Characterization and Evolution of Organized Shallow Convection in the Downstream North Atlantic Trades, Journal of Geophysical Research: Atmospheres, 126, e2021JD034575, https://doi.org/10.1029/2021JD034575, 2021.

Segal Rozenhaimer, M., Nukrai, D., Che, H., Wood, R., and Zhang, Z.: Cloud Mesoscale Cellular Classification and Diurnal Cycle Using a Convolutional Neural Network (CNN), Remote Sensing, 15, 1607, https://doi.org/10.3390/rs15061607, 2023.

Stevens, B., Vali, G., Comstock, K., Wood, R., van Zanten, M. C., Austin, P. H., Bretherton, C. S., and Lenschow, D. H.: POCKETS OF OPEN CELLS AND DRIZZLE IN MARINE STRATOCUMULUS, Bulletin of the American Meteorological Society, 86, 51-58, https://doi.org/10.1175/BAMS-86-1-51, 2005.

Tornow, F., Ackerman, A. S., and Fridlind, A. M.: Preconditioning of overcast-to-broken cloud transitions by riming in marine cold air outbreaks, Atmos. Chem. Phys., 21, 12049-12067, https://doi.org/10.5194/acp-21-12049-2021, 2021.

Vose, R. S., Easterling, D. R., and Gleason, B.: Maximum and minimum temperature trends for the globe: An update through 2004, Geophysical Research Letters, 32, https://doi.org/10.1029/2005GL024379, 2005.

Wang, H. and Feingold, G.: Modeling Mesoscale Cellular Structures and Drizzle in Marine Stratocumulus. Part I: Impact of Drizzle on the Formation and Evolution of Open Cells, Journal of the Atmospheric Sciences, 66, 3237-3256, https://doi.org/10.1175/2009JAS3022.1, 2009.

Wang, Q., Zhou, C., Zhuge, X., Liu, C., Weng, F., and Wang, M.: Retrieval of cloud properties from thermal infrared radiometry using convolutional neural network, Remote Sensing of Environment, 278, 113079, https://doi.org/10.1016/j.rse.2022.113079, 2022.

Watson-Parris, D., Sutherland, S. A., Christensen, M. W., Eastman, R., and Stier, P.: A Large-Scale Analysis of Pockets of Open Cells and Their Radiative Impact, Geophysical Research Letters, 48, e2020GL092213, https://doi.org/10.1029/2020GL092213, 2021.

Wood, R.: Stratocumulus Clouds, Monthly Weather Review, 140, 2373-2423, https://doi.org/10.1175/MWR-D-11-00121.1, 2012.

Wood, R. and Hartmann, D. L.: Spatial Variability of Liquid Water Path in Marine Low Cloud: The Importance of Mesoscale Cellular Convection, Journal of Climate, 19, 1748-1764, https://doi.org/10.1175/JCLI3702.1, 2006.

Wu, Y., Liu, J., Zhu, Y., Zhang, Y., Cao, Y., Huang, K.-E., Zheng, B., Wang, Y., Wang, Q., Zhou, C., Liang, Y., Wang, M., and Rosenfeld, D.: Global Classification Dataset of Daytime and Nighttime Marine Low-cloud Mesoscale Morphology [dataset], https://doi.org/10.5281/zenodo.13801408, 2024.

Wyant, M. C., Bretherton, C. S., Rand, H. A., and Stevens, D. E.: Numerical Simulations and a Conceptual Model of the Stratocumulus to Trade Cumulus Transition, Journal of the Atmospheric Sciences, 54, 168-192, https://doi.org/10.1175/1520-0469(1997)054<0168:NSAACM>2.0.CO;2, 1997.

Xue, H., Feingold, G., and Stevens, B.: Aerosol Effects on Clouds, Precipitation, and the Organization of Shallow Cumulus Convection, Journal of the Atmospheric Sciences, 65, 392-406, https://doi.org/10.1175/2007JAS2428.1, 2008.

Yamaguchi, T. and Feingold, G.: On the relationship between open cellular convective cloud patterns and the spatial distribution of precipitation, Atmos. Chem. Phys., 15, 1237-1251, https://doi.org/10.5194/acp-15-1237-2015, 2015.

Yuan, T., Song, H., Wood, R., Mohrmann, J., Meyer, K., Oreopoulos, L., and Platnick, S.: Applying deep learning to NASA MODIS data to create a community record of marine low-cloud mesoscale morphology, Atmos. Meas. Tech., 13, 6989-6997, https://doi.org/10.5194/amt-13-6989-2020, 2020.

Zhang, J., Liu, P., Zhang, F., and Song, Q.: CloudNet: Ground-Based Cloud Classification With Deep Convolutional Neural Network, Geophysical Research Letters, 45, 8665-8672, https://doi.org/10.1029/2018GL077787, 2018.